Amphiphilic gold nanoparticles perturb phase separation in multidomain lipid membranes

Ester Canepa,[a] Sebastian Salassi,[b] Anna Lucia de Marco,[b] Chiara Lambruschini, [a] Davide Odino,[b] Davide Bochicchio,[b] Fabio Canepa,[a] Claudio Canale,[b] Silvia Dante,[c] Rosaria Brescia,[d] Francesco Stellacci,[e] Giulia Rossi*[§a] and Annalisa Relini*[†a]

[a] Department of Chemistry and Industrial Chemistry, University of Genoa, Via Dodecaneso 31, 16146 Genoa, Italy.

[b] Department of Physics, University of Genoa, Via Dodecaneso 33, 16146 Genoa, Italy.

[c] Materials Characterization Facility, Italian Institute of Technology, Via Morego 30, 16163 Genoa, Italy.

[d] Electron Microscopy Facility, Italian Institute of Technology, Via Morego 30, 16163 Genoa, Italy.

[e] Institute of Materials, École Polytechnique Fédérale de Lausanne, Route Cantonale, 1015 Lausanne, Switzerland.

* Corresponding authors
§ *rossig@fisica.unige.it*
† *relini@fisica.unige.it*

Electronic Supplementary Information

The material of this Electronic Supplementary Information (ESI) is presented following the order in which it is recalled by the main text of the paper.

Synthesis of amphiphilic and negatively charged Au NPs (NP–)
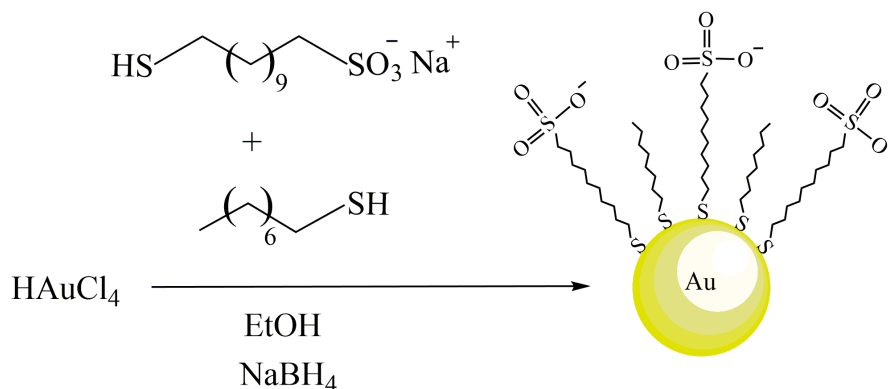
Figure S1. One-phase protocol. Schematic drawing illustrating the procedure used to synthesize NP– coated by 1-octanethiol (OT) and 11-mercaptoundecane sulfonate (MUS).

Before adding all chemicals, the solvent ethanol was purged in argon for almost 30 min and all the steps thereafter were performed in a gently purged argon environment. $HAuCl_4 \cdot 3H_2O$ (0.225 mmol) was dissolved in ethanol (45 mL) at 0 °C in a 250 ml two neck round bottom flask. The solution was stirred with a magnetic bar on a stirring plate till the complete dissolution of the salt. A thiol mixture (0.225 mol), composed of 1-octanethiol (OT, 0.075 mmol) and 11-mercaptoundecane sulfonate (MUS, 0.15 mmol), was prepared in anhydrous methanol (5 mL). After sonication to ensure complete dissolution and mixing of ligands, the thiol solution was added to the gold solution and stirred together for 15 min before the addition of the reducing agent. During this waiting, the color change of the gold mixture from transparent yellow to turbid yellowish indicated the formation of a gold-thiolate complex. $NaBH_4$ (2.5 mmol) was dissolved in ethanol (50 mL, 0 °C) and slowly added dropwise by using a syringe needle (flux speed: 1.25 mL min^{-1}). Upon addition, the gold-thiol solution slowly darkened to reddish-black. After the complete addition of $NaBH_4$, the solution was stirred for 3 h. The reaction mixture was then placed in the refrigerator (-21 °C) to precipitate the NP– overnight. The precipitate was washed by repeated precipitation in ethanol, methanol, and acetone, and finally dried under high vacuum thus obtaining a shiny dark powder.

Characterization results of NP size distribution (TEM) and NP ligand composition (NMR) are shown in Figure S13 and S17, respectively. DLS and ζ-potential results are reported in Table S5.

AFM results: multidomain membrane morphology before the interaction with NP–

GM1-containing M1 membranes (neuronal model membranes)
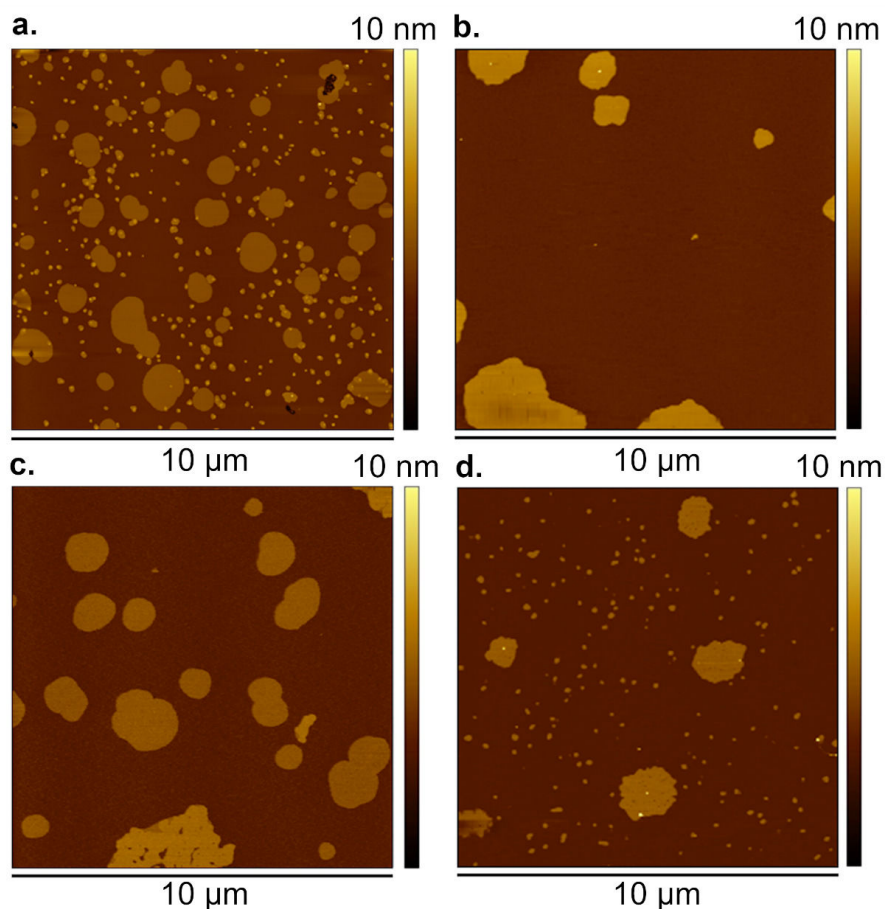
Figure S2. Formation of ordered and disordered domains by segregation of lipid species in planar SLBs with composition M1. These AFM images show the variability in domain morphology and size in multidomain supported lipid bilayers (SLBs) before the interaction with NP–. In some cases, ordered domains exhibit protruding subdomains which can be assigned to regions with higher GM1 concentration. This behavior has already been observed in SLBs formed by mixtures DOPC:SM:chol:GM1.[1]
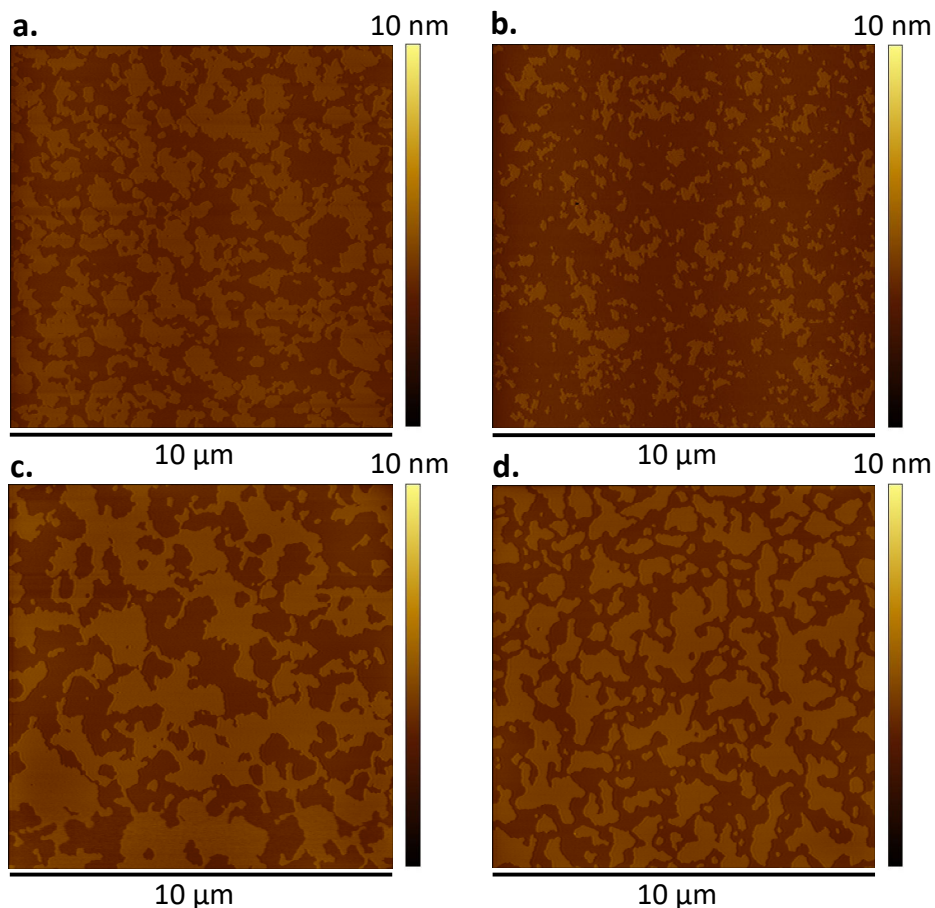
Figure S3. Formation of ordered and disordered domains by segregation of lipid species in planar SLBs with composition M2 and M3. a and **b** refer to composition M2, **c** and **d** refer to composition M3. Also these AFM images show the variability in domain morphology and size in multidomain SLBs before the interaction with NP–.

Height difference (Δz) between ordered and disordered domains in M2 and M3 SLBs

Composition	Δz [nm]
M2	0.97 ± 0.11
M3	1.07 ± 0.13

Table S1. Δz in M2 and M3 membranes. As for M1 SLBs, Δz was calculated counting at least 200 values on 5 different AFM images. Average mean values are reported with their standard deviation. Δz histograms are shown in Figure S4.
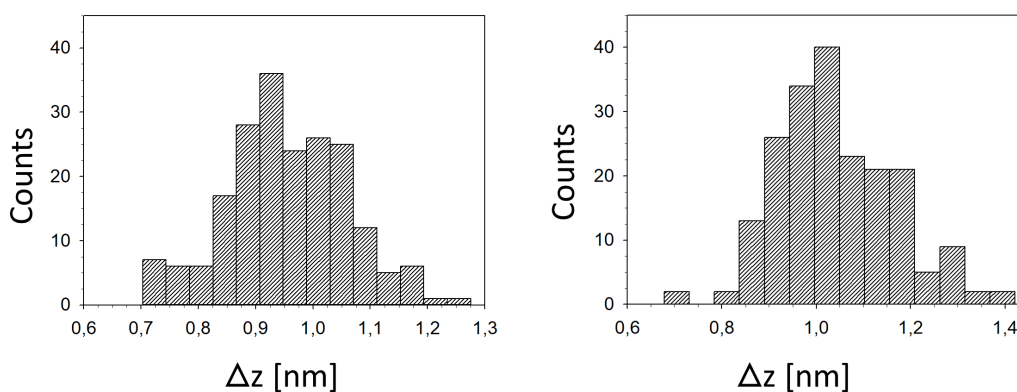
Figure S4. Δz distribution between ordered and disordered domains in M2 (left) and M3 (right) membranes. Mean values are reported in Table S1.

Computational results: equilibration of the Lo – Ld phase separation
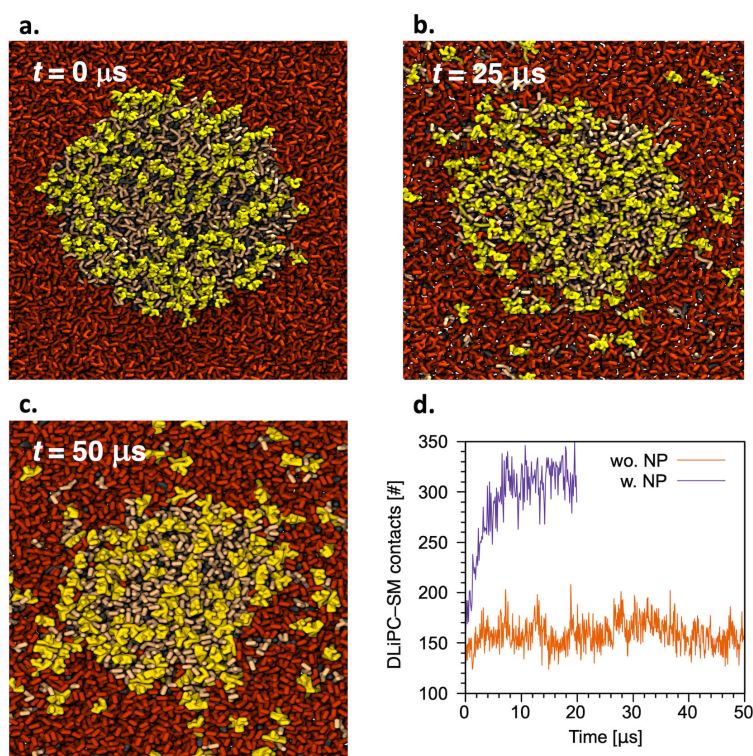
Figure S5. Lo domain stability in MD simulations. a We constructed a preformed a Lo domain and **b**, **c** let it adjust and equilibrate for 50 µs. The system composition is a mixture of 1,2-dilinoleoyl-*sn*-glycero-3-phosphocholine (DLiPC), sphingomyelin (SM), cholesterol (chol) and ganglioside GM1, in the proportion DLiPC:SM:chol:GM1 56:18:17:9. The Lo domain remains stable and well defined for all the 50 µs (**c**), as it can be seen also by looking at the number of contacts between DLiPC and SM as a function of time (**d**, orange curve). As a comparison, we added in **d** also the DLiPC-SM contacts after the insertion of a NP− (dark purple curve). In this case, the contacts increase significantly, and this corresponds to an almost complete destruction of the phase separation.

Experimental sample preparation: study of the NP-membrane interaction

AFM sample preparation
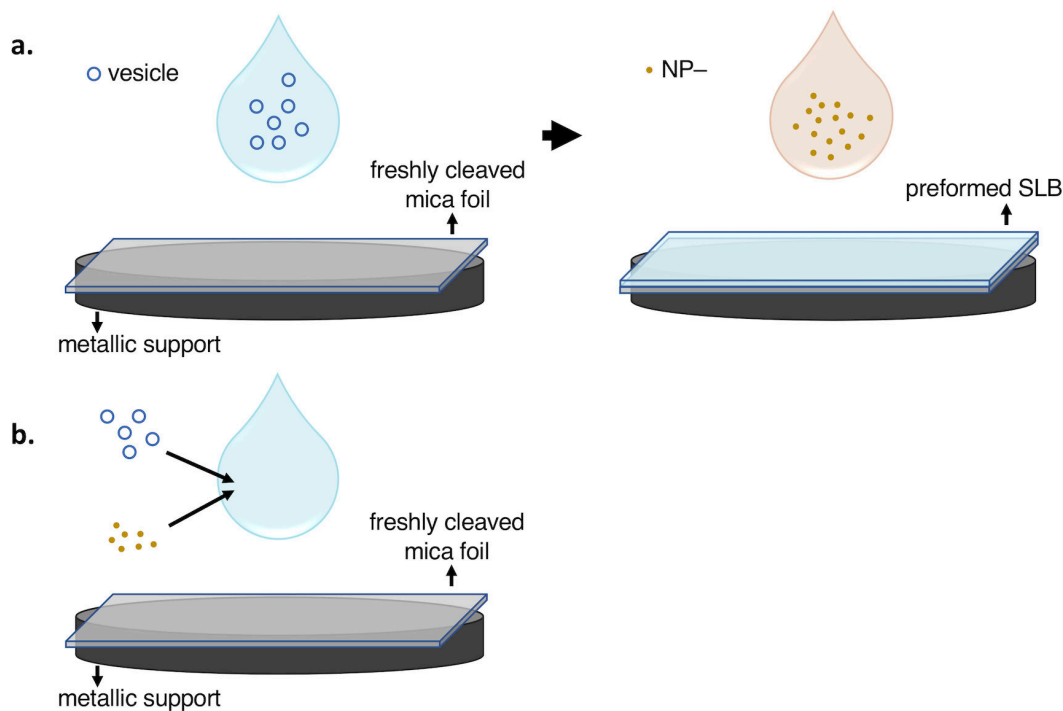
Figure S6. Schematic drawing illustrating the two sample preparation methods for AFM imaging. AFM samples containing NP– were prepared following two different protocols: **a** the *incubation method* and **b** the *pre-incubation method*. In **a**, NP– were incubated on a preformed multidomain SLB deposited onto a freshly cleaved mica foil. In **b**, NP– were pre-incubated with multidomain lipid vesicles before their deposition on mica and subsequent formation of the final SLB.

QCM-D sample preparation. The same protocols shown in Figure S6 were applied to the preparation of QCM-D samples containing NP– (in this case the solid substrate is the sensor).

AFM results: NP– adsorb on the disordered phase
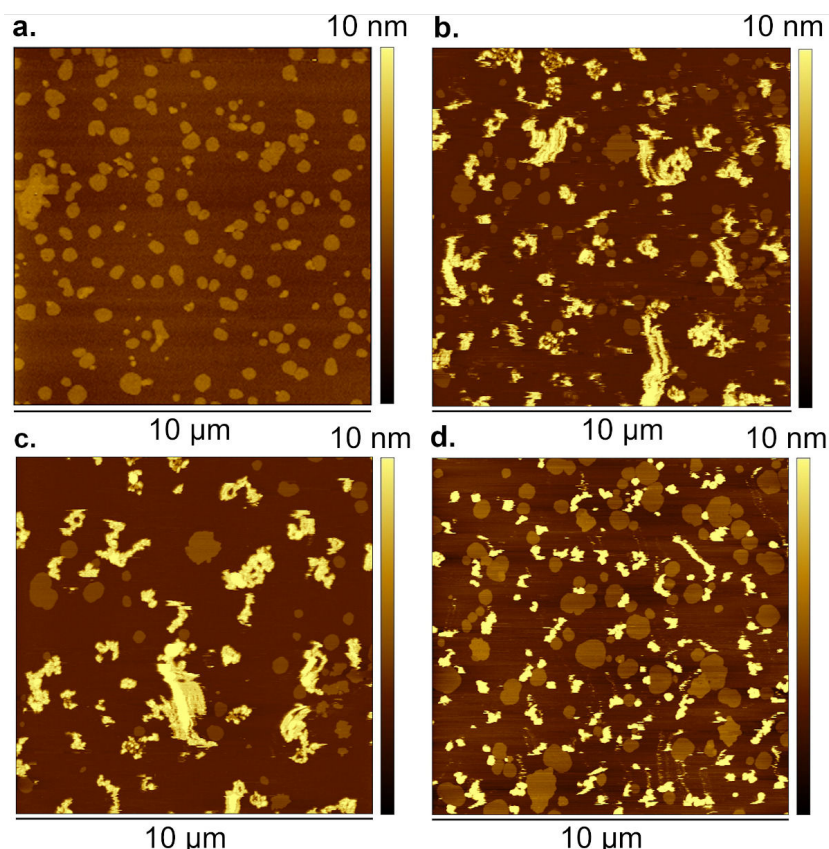
Figure S7. Effect of NP– incubation on preformed M1 SLBs. NP– cluster formation on multidomain M1 SLBs is a time-dependent phenomenon. AFM images were acquired **a** 40 min; **b** ~ 17 h; **c** ~ 18 h; **d** ~ 22 h after the addition of NP– (20 μL, 0.12 mg mL^{-1}). NP– clusters are higher (i.e., lighter in color) than ordered domains. NP– aggregates do not form in the time scale of minutes (**a**), only after several hours NP– clusters adsorbed on the disordered phase were imaged, without observing significant changes within 5 h (**b**-**d**). As for the ordered domains, also for NP– clusters a sample-dependent variability in size and density can be observed.

QCM-D results: quantification of lipid/NP– ratio in pre-incubated GM1-containing M1 membranes

As mentioned in the main text, we used the QCM-D results to quantify the ratio between lipid molecules and embedded NP– in M1 membranes pre-incubated for 4 h (see main text, Figure 4). The quantification was performed as follows. The mass of a spherical NP– with diameter d_{core} = 2.7 nm and ligand composition MUS:OT 80:20 is m_{NP} = 1.6 10^{-10} ng (MW_{NP} = 96062 g mol^{-1} estimated by the computational model), then the number of embedded NP– is obtained as $\Delta m/m_{NP}$ ~ 0.017 NP– nm^{-2}. Concerning the lipids, the SLB areal mass calculated from the frequency shift (26 Hz) was 463 ng cm^{-2}; this mass includes a water layer that has been determined to be ~ 102 ng cm^{-2},[2,3] which leaves an areal mass for the lipid bilayer of 361 ng cm^{-2}. The average molecular weight of the lipid mixture is 813.14 g mol^{-1}, corresponding to a molecular mass 1.35 10^{-12} ng molecule^{-1}. Dividing the areal mass of the SLB by the mass of a single lipid molecule, we estimated that there are 2.67 molecule nm^{-2} on the bilayer or 1.34 molecule nm^{-2} on the lipid monolayer; this value corresponds to a lipid area a_L = 0.75 nm^2 molecule^{-1}, in agreement with the structural data in the literature.[4] The ratio between

the number of lipid molecules and the number of embedded NP– is therefore 1.34/0.017 = 79 lipids/NP–.

On the other hand, the AFM investigation showed an ordered lattice of NP– with a NP-NP distance d = 7.5 nm (main text, Figure 6a, b). This value is confirmed by simulations (inset of Figure 7c). Assuming a hexagonal unit cell, the unit cell area is 49 nm^2 which, divided by the lipid area, gives 65 lipid molecules/NP–. This value is not far from, but smaller than the estimation based on the adsorbed mass. In fact, the latter estimation takes into account the total amount of lipid molecules in the SLB, including those not involved in the ordered NP– lattice, thus resulting in a larger lipid/NP– ratio.

Membrane rigidity disfavors NP– embedding into the membrane core

Pre-incubation of NP– with GM1-free M2 bilayers
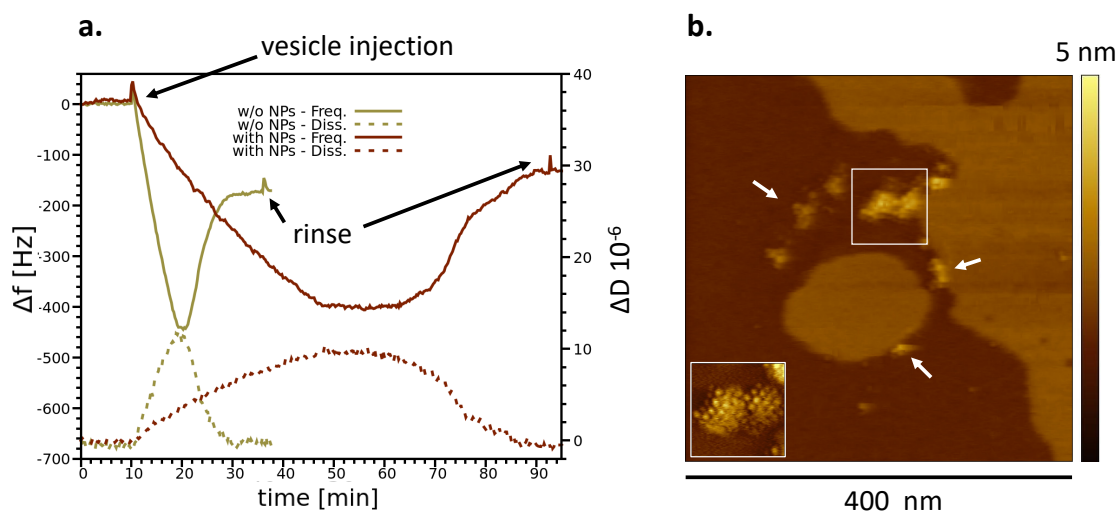
Figure S8. Larger membrane rigidity disfavors NP– uptake in M2 membranes. a QCM-D data indicating little to no uptake of NP– in the M2 bilayer after pre-incubation of 4 h (7th overtone). Frequency variation (continuous lines), Δf, and dissipation variation (dotted lines), ΔD. The slow deposition kinetics of the pre-incubated vesicles on the QCM-D support is consistent with the presence of NP– reversibly adsorbed at the surface of the vesicles, but not fully embedded into the membrane core. **b** M2 bilayer imaged by AFM after 4h of pre-incubation with NP– (20 μL, 0.12 mg mL^{-1}). Only sparse, little NP– clusters can be found in the sample. In particular, NP– are both in the disordered phase and at the ordered – disordered boundaries. The inset shows a zoomed AFM scan of the NP– cluster framed in the image. Other NP– clusters are indicated by white arrows.

QCM-D results on M2 membranes pre-incubated with NP–. The graph in Figure S8a compares the traces obtained with multidomain lipid vesicles without GM1 alone and pre-incubated with NP–. At variance with the M1 case shown in the main text, Figure 4, the frequency shifts are similar both when vesicles attached to the sensors (i.e., in correspondence to the continuous line minima) and when the SLBs formation was completed (i.e., after reaching the plateau at the end of the recording). The normalized frequency shifts at the plateau are ≈ 25 Hz; these values are consistent with the formation of a SLB, and comparable to the value obtained in the presence of GM1. In the case of M2 vesicles pre-incubated with NP–, the plateau value is slightly lower than that of M2 vesicles alone. This may be due to the presence of holes in the supported bilayer that have often been observed during

AFM imaging on pre-incubated M2 membranes. Since no difference in the adsorbed mass was detected in the presence and in the absence of NP–, little or no insertion of NP– in the bilayer has occurred. However, the kinetics of vesicles adsorption and rupture was slower in the presence of NP–. This fact could indicate a weak interaction of NP– with the hydrophilic headgroups of the bilayer. NP– adsorbed at the surface of the vesicles, not penetrating the membrane core, may indeed affect the interaction of the vesicles with the sensor.

Computational results: NP– favorably adsorb on Ld and homogeneous melted phase
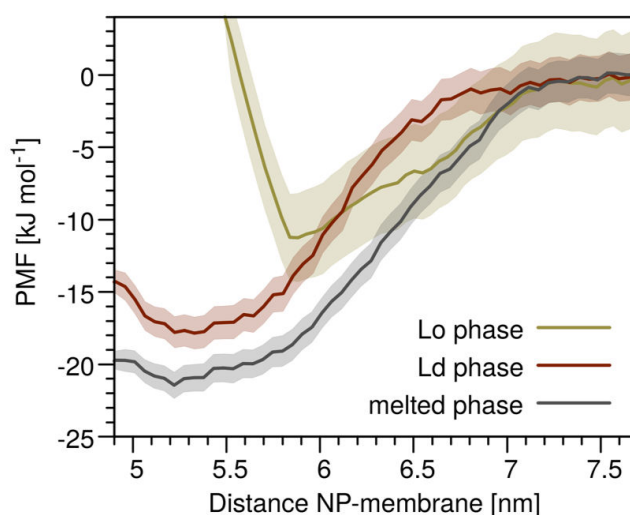
Figure S9. Adsorption of a 4 nm NP– on the different phases (M1 membrane composition). Potential of mean force (PMF) profiles for the adsorption of a single NP– onto Ld, Lo and melted phase of M1 membranes. The adsorption of the NP– on a bilayer without lateral phase separation (melted phase) is thermodynamically favored with respect to the adsorption on both the Ld and Lo phases.

Thermodynamics of NP-induced lipid mixing in phase-separated bilayers

Enthalpic effect of NP insertion into different mixtures. As described in the main text, we compared via MD simulations the energetics of the bilayers with composition M1 and M3 with and without different types of embedded NPs. M1 bilayers were composed of 2850 lipids, while M3 bilayers comprised 3520 lipids. As for the NP types, we considered the NP– and the fully hydrophobic C_{60} fullerenes.[5]

We considered NP–@M1, NP–@M3, and C_{60}@M1 combinations. For each bilayer/NP combination, we ran 4 simulations sampling 4 different configurations:
- the lipid mixture in a random arrangement;
- the lipid mixture in a random arrangement with an embedded NP;
- the lipid mixture in its phase-separated state;
- the lipid mixture in its phase-separated state with an embedded NP.

Simulation set up. The membranes (both in a random arrangement and phase-separated) were generated using the *insane.py* script.[6] The equilibrium configurations (phase-separated state, S) were equilibrated until the contacts between the different lipid species were constant, while out of

equilibrium configurations (mixed state, M) were equilibrated for just 200 ns to avoid their spontaneous transition toward the phase separated state. We remark that this spontaneous transition is extremely slow on the simulation time scale, typically requiring tens of microseconds to fully converge. NPs were inserted by creating a hole in the bilayers with position restraints, and then letting the hole close spontaneously around the NP. All systems have been equilibrated for 200 ns. After equilibration, enthalpies have been averaged over 200 ns of unbiased MD run by means of the *gmx energy* Gromacs tool.

Results and analysis. The enthalpic difference between M and S, without NPs, can be split into lipid-lipid (l-l), lipid-solvent (l-w), and solvent-solvent (w-w) interactions (water and ions have been grouped together and treated as solvent):

$$\Delta H_{S \to M} = (H_{l-l,M} - H_{l-l,S}) + (H_{l-w,M} - H_{l-w,S}) + (H_{w-w,M} - H_{w-w,S})$$

Analogously, for the case with NPs, the enthalpic difference can be split into lipid-lipid (l-l), lipid-NP (l-NP), lipid-solvent (l-w), NP-solvent (NP-w), NP-NP, and solvent-solvent (w-w) interactions:

$$\Delta H_{S \to M}^{NP} = (H_{l-l,M}^{NP} - H_{l-l,S}^{NP}) + (H_{l-NP,M}^{NP} - H_{l-NP,S}^{NP}) + (H_{NP-NP,M}^{NP} - H_{NP-NP,S}^{NP})$$
$$+ (H_{l-w,M}^{NP} - H_{l-w,S}^{NP}) + (H_{NP-w,M}^{NP} - H_{NP-w,S}^{NP}) + (H_{w-w,M}^{NP} - H_{w-w,S}^{NP})$$

where the *NP* superscript indicates the presence of NPs in the bilayer. Solvent-solvent and NP-NP enthalpy differences are negligible. In Table S2 we report the values of the overall enthalpy differences as obtained from the simulations. We considered M1 and M3 membranes and two types of NP, NP– and C_{60} fullerene.

Membrane composition	$\Delta H_{S \to M}$ [kJ mol^{-1}]	NP type (NP/lipid molar ratio in simulation)	$\Delta H_{S \to M}^{NP}$ [kJ mol^{-1}]	Model prediction	Experimental validation
M1 DLiPC:SM:chol:GM1 56:18:17:9	+9.96 10^3	NP– (0.35 10^{-3})	-1.2 10^3	destabilize phase separation already at low concentration	this work (main text, Figure 5a-c)
M3 DLiPC:DPPC:chol 40:40:20	+4.9 10^3	NP– (0.28 10^{-3})	+1.9 10^3	destabilize phase separation as concentration increases	this work (Figure S10)
M1 DLiPC:SM:chol:GM1 56:18:17:9	+9.96 10^3	C_{60} fullerene (1.8 10^{-2})	+1.48 10^4	stabilize phase separation	this work (Figure S11) and ref.[7]

Table S2. **Enthalpies of M1 and M3 bilayers with and without an embedded NP– or C_{60} fullerene.** Our model, validated against experimental data taken from this work and from the literature, correctly predicts the effect of NPs on lipid lateral phase separation. Total enthalpy differences were calculated via averaging over 200 ns of unbiased MD simulations.

1. *M1 membranes and NP–*. The first row in Table S2 refers to the case of NP– in M1 bilayers. Here, our simulations suggest that the disruption of phase separation may take place already at lower concentration than that used for the vesicle pre-incubation of 4 h (see main text, Figure 5b). Indeed, our experimental results show that the ordered – disordered phase

separation blurs already after 10 min of pre-incubation of vesicles and NP– (main text, Figure 5a), and fully disappears after 4 h of pre-incubation.

2. *M3 membranes and NP–*. The second row of Table S2 refers to the case of NP– in M3 bilayers. Here, $\Delta H > \Delta H^{NP}$ but ΔH^{NP} remains positive at the NP concentration used in the simulations, meaning that the destabilization of phase separation may be achieved only at sufficiently high NP– concentration. We checked this by introducing 1 or 2 NP– in the simulated M3 bilayer: Table S3 shows the effect of increasing NP concentration in the simulated M3 bilayer, confirming that the stability of the phase separation decreases as c_{NP} increases. Experimentally, after 4 h of pre-incubation with NP–, M3 bilayers show only a little uptake of NP–. Small NP aggregates can be spotted in the AFM samples, which still show the presence of ordered – disordered phase separation, as reported in Figure S10.

	no NP–	*1 NP–*	*2 NP–*
DLiPC-DPPC contacts	126 ± 1	144 ± 2	161 ± 2

Table S3. Number of DLiPC-DPPC contacts in a simulated M3 membrane containing no NP–, 1 NP– and 2 NP–. We equilibrated the three systems for 5 µs and then averaged the number of DLiPC-DPPC contacts over 10 µs, the reported error is the standard deviation.
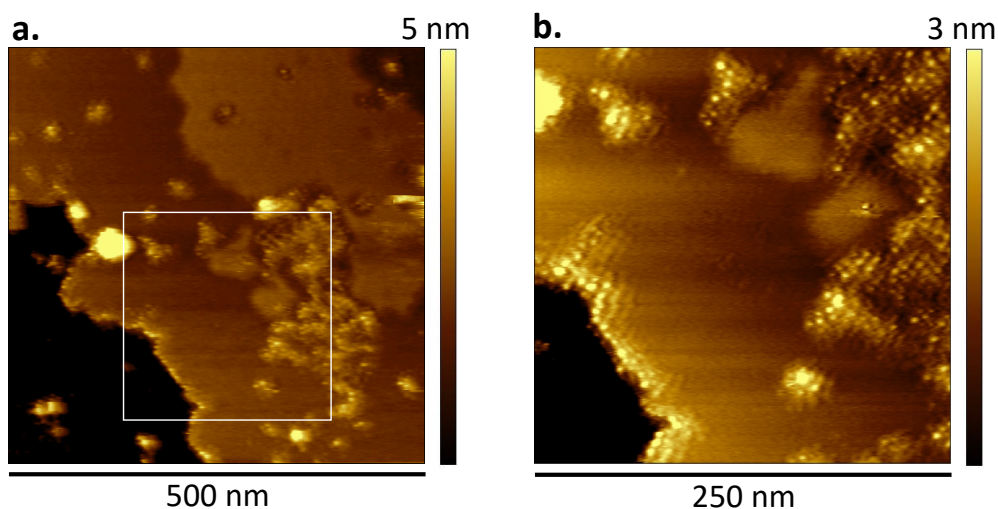
Figure S10. A low NP– uptake in M3 membranes does not alter phase separation. a M3 bilayer imaged by AFM after 4 h of pre-incubation with NP– (20 µL, 0.12 mg mL⁻¹). The dark region in the bottom right corner represents a hole in the SLB. NP– accumulate at bilayer edges (as already observed in homogeneous bilayers[8]), in the disordered phase, and at the ordered – disordered boundaries (as observed for M2 membranes in Figure S8b). The low NP– uptake does not allow for the alteration of phase separation as predicted by MD simulations. **b** Zoomed AFM scan corresponding to the frame in **a**.

3. *M1 membranes and C_{60} fullerene*. The third row in Table S2 refers to the case of C_{60} fullerenes embedded in our M1 bilayer. Fullerenes increase the enthalpic advantage of the phase separated state over the mixed state, thus stabilizing the phase separation. Figure S11 shows the phase stabilization as obtained in our simulations. The distribution coefficients of

fullerenes in a similar ternary mixture, DOPC:SM:chol, measured by Ha et al.,[7] confirm that fullerenes do not induce lipid mixing.

Table S4 details the splitting of the enthalpy differences into lipid-lipid, lipid-water, lipid-NP, and NP-water contributions.
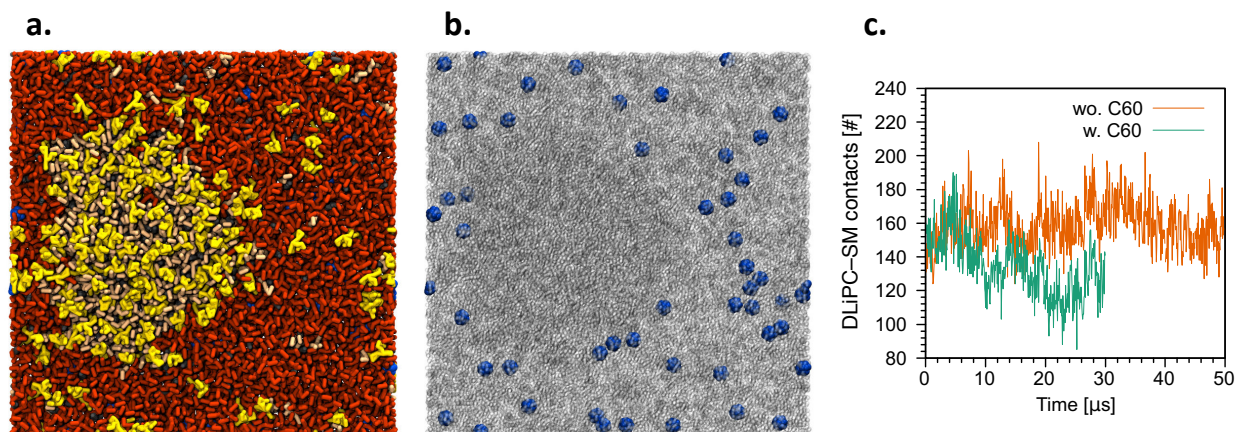
Figure S11. Unbiased MD simulations of C_{60} fullerenes in M1 bilayers. In **a** and **b** a snapshot of a phase-separated M1 bilayer with embedded C_{60} fullerenes ($1.8 \cdot 10^{-2}$ C_{60}/lip molar ratio), at equilibrium. The two images refer to the same simulation snapshot. In **a**, the lipid phase separation can be appreciated. In **b**, lipids are made transparent to make the blue C_{60} visible. In **c** the effect of C_{60} is not to alter, but stabilize phase separation.

	$\Delta H_{S \to M}$ [kJ mol^{-1}]			$\Delta H_{S \to M}^{NP}$ [kJ mol^{-1}]				
	l-l	l-w	total	l-l	l-w	l-NP	NP-w	total
NP– @ M1								
	$2.02 \cdot 10^4$ $\pm 0.03 \cdot 10^4$	$-1.02 \cdot 10^4$ $\pm 0.03 \cdot 10^4$	**$1.00 \cdot 10^4$** $\pm 0.04 \cdot 10^4$	$6.7 \cdot 10^3$ $\pm 0.2 \cdot 10^3$	$-6.6 \cdot 10^3$ $\pm 0.3 \cdot 10^3$	$-1.32 \cdot 10^3$ $\pm 0.04 \cdot 10^3$	0 ± 10	**$-1.2 \cdot 10^3$** $\pm 0.3 \cdot 10^3$
NP– @ M3								
	$7.7 \cdot 10^3$ $\pm 0.3 \cdot 10^3$	$-2.8 \cdot 10^3$ $\pm 0.4 \cdot 10^3$	**$4.9 \cdot 10^3$** $\pm 0.6 \cdot 10^3$	$5.7 \cdot 10^3$ $\pm 0.4 \cdot 10^3$	$3.5 \cdot 10^3$ $\pm 0.5 \cdot 10^3$	-150 ± 90	-180 ± 70	**$1.9 \cdot 10^3$** $\pm 0.6 \cdot 10^3$
C_{60} @ M1								
	$2.02 \cdot 10^4$ $\pm 0.03 \cdot 10^4$	$-1.02 \cdot 10^4$ $\pm 0.03 \cdot 10^4$	**$9.96 \cdot 10^3$** $\pm 0.03 \cdot 10^3$	$1.68 \cdot 10^4$ $\pm 0.03 \cdot 10^4$	$-1.8 \cdot 10^3$ $\pm 0.4 \cdot 10^3$	-143 ± 5	-26 ± 1	**$1.48 \cdot 10^4$** $\pm 0.05 \cdot 10^4$

Table S4. Splitting of enthalpy differences into lipid-lipid (l-l), lipid-water (l-w), lipid-nanoparticle (l-NP), and nanoparticle-water (NP-w) contributions, calculated via averaging over 200 ns of unbiased MD simulations, the reported error is the standard error.

AFM results: NP– form ordered supramolecular lattices within the M1 bilayer
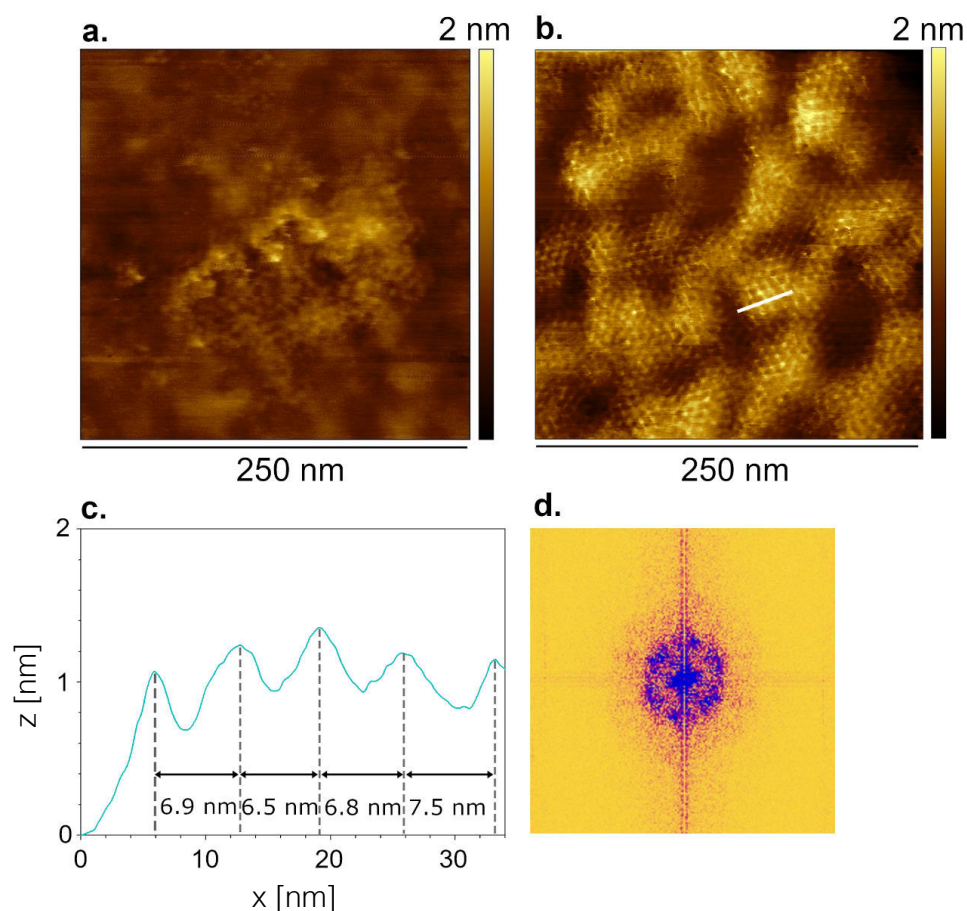
Figure S12. NP– form ordered supramolecular aggregates after phase separation perturbation in M1 bilayers. a Small patch of the NP– lattice, isolated within the bilayer, formed after a short pre-incubation time (10 min) (20 μL of NP–, 0.12 mg mL^{-1}). **b** Only after longer pre-incubation times (e.g., 4 h), the periodic NP– lattice tends to uniformly cover most of the bilayer surface. **c** Height profile of the ordered NP– row along the white line in **b**. Dashed grey lines indicate the periodic NP-NP distance, whose mean is 7.5 ± 0.1 nm. The average Δz between the supramolecular lattice and the disordered phase is 1.2 nm (with standard deviation of 0.3 nm). **d** 2D Fourier transform of the image in panel **b**, highlighting the periodicity of the NP– lattice.

BF-TEM and DLS characterizations of NP–
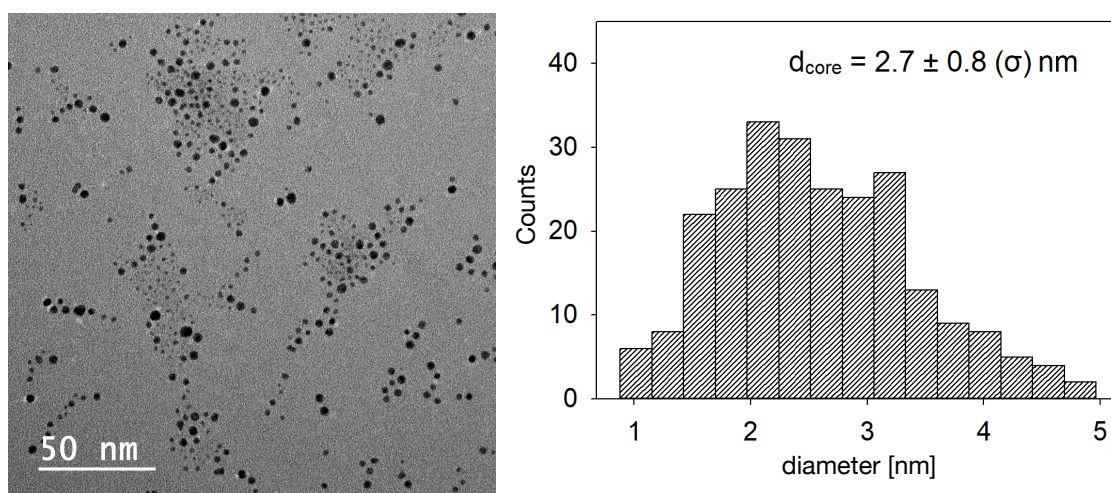
Figure S13. TEM characterization. Left: bright-field TEM image of NP–. Right: histogram of the experimental size distribution. For the BF-TEM characterization, the NP– mean diameter and standard deviation (σ) were calculated by assuming spherical morphology and by counting at least 300 particles with ImageJ software.

TEM and DLS sample preparation. TEM sample was prepared by suspending a small amount of NP– in Milli-Q water. After sonication in a bath-type sonicator, few drops of the diluted dispersion were deposited onto an ultrathin carbon-coated Cu grid. The same diluted dispersion was used for DLS characterizations.

Results on BF-TEM and DLS analyses are reported Table S5. Due to the highly negative ζ, all NP– dispersions showed great stability in time. DLS size characterization was repeated before each experiment for additional control.

d_{core} [nm]	d_h [nm]	ζ [mV]
2.7 ± 0.8 (σ)	6.5 ± 0.2	-51 ± 5

Table S5. BF-TEM (d_{core}), hydrodynamic diameter (d_h) and ζ-potential (ζ) characterization of NP–. For DLS size results, we considered the number distributions. We calculated the uncertainty on the mean value on 23 measurements; in the case of ζ-potential, we used 9 measurements. For both hydrodynamic diameter and ζ-potential measurements, the uncertainties correspond to the 95 % confidence intervals of Student's t-distributions.

Computational results: dimerization of NP– increases ligand conformational space
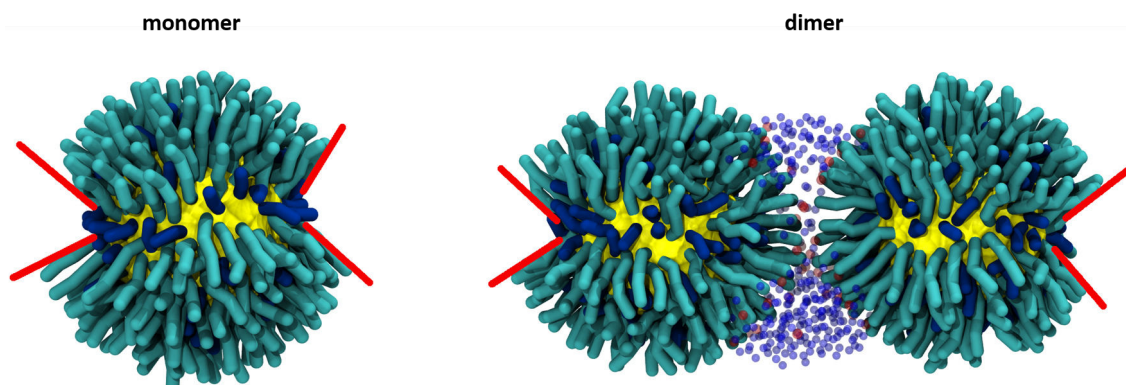
Figure S14. Configuration of the ligands of a 4 nm NP– in its monomeric or dimeric state. The hydrophilic ligands (cyan) of the 4 nm NP– snorkeled inside a bilayer assume the configuration shown on the left: they are all oriented toward the lipid heads in the upper or lower layer. However, when two NP– form a stable dimer and a pore spontaneously appears between them, the ligands rearrange as shown on the right. In the proximity of the pore (water shown as transparent blue beads, ions shown as transparent red beads) the hydrophilic ligands of the two NP– can now occupy also the space between the NP–. Anionic hydrophilic ligands (MUS) in cyan, hydrophobic ligands (OT) in blue, Au atoms in yellow. Water in transparent blue beads and ions in transparent red beads.

Computational results: nanopores stabilize NP– aggregation
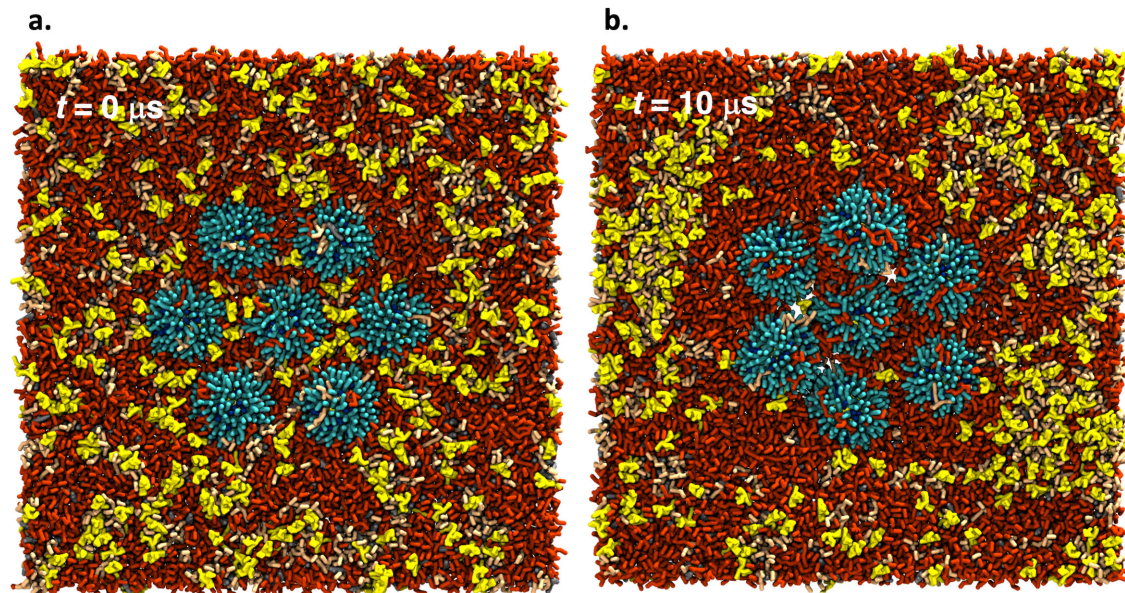
Figure S15. Simulation of a preformed NP– hexagonal lattice. We constructed a NP hexagonal lattice formed by 7 NP– (4 nm of diameter) and let it equilibrate for 10 μs. The hexagonal configuration remains stable, and pores are formed between the NP–.

Movie S1. Movie of the hexagonal aggregate formation. We used a starting configuration in which 7 NP− do not interact with each other (main text, Figure 7d), with the aim to assess if an ordered lattice can spontaneously form. After ~ 23 μs of unbiased run, the NP− form a stable hexagonal aggregate, in which the NP-NP distance nicely match the experimental data.

Synthesis and purity characterization of the anionic ligand 11-mercapto-1-undecanesulfonate

All the chemicals indicated in this protocol were purchased from Sigma Aldrich and used without further purification unless specified. Sodium 11-mercapto-1-undecanesulfonate (MUS) was prepared according to a modified literature procedure[9,10] (Figure S16). In particular we have optimized the thiol-ene reaction (step 2) and we have calculated the purity of MUS by quantitative nuclear magnetic resonance (qNMR).
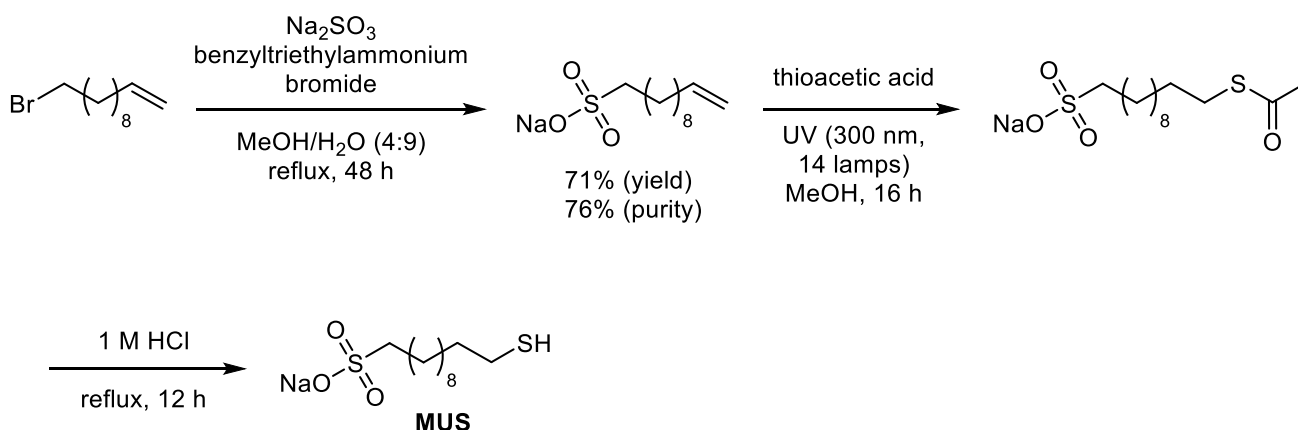
Figure S16. Scheme of the synthesis of the anionic ligand 11-mercapto-1-undecanesulfonate (MUS).

1. Sodium undec-10-ene-1-sulfonate
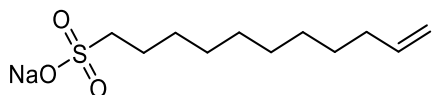
To a solution of sodium sulphite (5.77 g, 184.5 mmol) in a mixture of MeOH (40 mL) and Milli-Q water (90 mL) was added benzyltriethylammonium bromide (13 mg, 0.05 mmol) and 11-bromo-1-undecene (5 mL, 22.8 mmol). The resulting solution was stirred for 48 h under reflux, then it was extracted with Et_2O (80 mL × 5), the aqueous layer was evaporated, and the resulting white solid was further dried under high vacuum. To remove inorganic salts, the solid was suspended in MeOH (150 mL) and the solution collected after filtration was evaporated. This step was repeated twice, and the desired product was obtained as white solid (4.176 g, yield 71 %, purity qNMR 76 %) and directly used in the next step. ^1H NMR (300 MHz, D_2O) δ 5.79 (ddt, J = 17.0, 10.2, 6.7 Hz, 1H, C<u>H</u>=CH$_{cis}$H$_{trans}$), 4.92 (ddt, J = 17.3, 2.2, 1.6 Hz, 1H, CH=CH$_{cis}$<u>H</u>$_{trans}$), 4.84 (ddt, J = 10.2, 2.4, 1.1 Hz, 1H, CH=C<u>H</u>$_{cis}$H$_{trans}$), 2.83 – 2.67 (m, 2H, CH$_2$C<u>H</u>$_2$SO$_3$Na), 1.98 – 1.83 (m, 2H, C<u>H</u>$_2$CH=CH$_2$), 1.68 – 1.50 (m, 2H, C<u>H</u>$_2$CH$_2$SO$_3$Na), 1.36 – 1.08 (m, 12H, 6×CH$_2$).

2. Sodium 11-(acetylthio)undecane-1-sulfonate
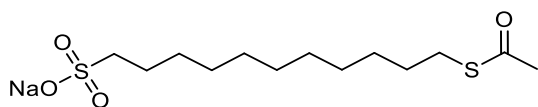
To a solution of sodium undec-10-ene-1-sulfonate (4.176 g, 16.28 mmol) in dry MeOH (75 mL, previously degassed with nitrogen) in a Pyrex tube under N_2 atmosphere was added thioacetic acid

(4.03 mL, 56.4 mmol). The tube was placed into the Rayonet apparatus and irradiated under stirring at 300 nm for 16 h (14 lamps, 8 W each) (see Table S6 for the optimization of this step). Then the solvent was evaporated and the excess of thioacetic acid was remove with *n*-heptane (5 mL × 4). The resulting beige solid was washed with Et$_2$O (30 mL × 4) obtaining a white solid that was dried under high vacuum. The product dissolved in MeOH (40 mL) by sonication and was further purified by adding active charcoal (600 mg). After stirring for 2 h, the charcoal was removed by filtration through a Celite plug and the solvent was evaporated. The desired product was obtained as white solid (6.588 g) and used directly in the next step. ^{1}H NMR (300 MHz, D$_2$O) δ 3.00 – 2.81 (m, 4H, 2×CH$_2$C$\underline{H}_2$S), 2.38 (s, 3H, C$\underline{H}_3$CO), 1.84 – 1.67 (m, 2H, C$\underline{H}_2$CH$_2$S), 1.60 (p, *J* = 7.1 Hz, 2H, C$\underline{H}_2$CH$_2$S), 1.51 – 1.22 (m, 14H, 7×CH$_2$).

Entry	Number of lamps [300 nm]	Time	Conversion [^{1}H NMR]
1	8	14 h	60 %
2	15	20 h	100 %
3	**14**	**16 h**	**100 %**

Table S6. Optimization of the reaction time and number of lamps for the thiol-ene reaction. For this step, we used a Rayonet apparatus. The optimized combination is reported in bold.

3. *Sodium 11-mercapto-1-undecanesulfonate (MUS)*
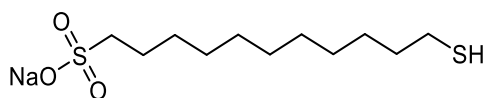
A solution of sodium 11-(acetylthio)undecane-1-sulfonate (6.588 g, 19.8 mmol) in 1 м HCl (75 mL) was stirred under reflux for 12 h. The mixture was cooled at 0 °C, then Milli-Q water (75 mL) and 1 м NaOH (35 mL) were added. The mixture was kept at 4 °C overnight and the resulting suspension was centrifuged (6500 rpm, 45 min). The solid was collected and dried under high vacuum in the presence of P$_2$O$_5$, while the supernatant was subjected to three subsequent crystallizations and more product was obtained. The purity was checked for each batch (Table S7) and the purest was used for the synthesis of NP– (purity qNMR 93 %). The qNMR protocol is reported in the next paragraph. ^{1}H NMR (300 MHz, D$_2$O) δ 2.84 – 2.67 (m, 2H, CH$_2$C$\underline{H}_2$S), 2.41 (t, *J* = 7.1 Hz, 2H, CH$_2$C$\underline{H}_2$S), 1.69 – 1.54 (m, 2H, C$\underline{H}_2$CH$_2$S), 1.48 (p, *J* = 7.1 Hz, 2H, C$\underline{H}_2$CH$_2$S), 1.36 – 1.08 (m, 14H, 7×CH$_2$).

Batch	Purity [qNMR]
1	82 %
2	**93%**
3	84 %
4	87 %

Table S7. Purities of final MUS batches. The batch used for NP– synthesis is reported in bold.

Characterization of MUS purity: qNMR protocol

The sample MUS (ca. 10 mg) and the internal standard 3-(trimethylsilyl)propionic-2,2,3,3-d_4 acid sodium salt (TMSP, ca. 10 mg) were precisely weighted into a vial, then D_2O (600 µL) was added and the mixture was sonicated for 10 min. The clear solution was transferred into a 5 mm NMR tube and ^1H NMR spectrum was acquired (delay: 60 s, acquisition time: 4 s, number of scans: 64). Post-acquisition processing was performed with MestReNova (Mestrelab research v. 11.0): manual phase correction, 264 k zero filling, 5rd order polynomial baseline correction, apodization LB = 0.1 Hz and manual integration. The purity was calculated by applying the following equation:

$$P\% = \frac{n_{ISTD} \cdot Int_t \cdot MW_t \cdot m_{ISTD}}{n_t \cdot Int_{ISTD} \cdot MW_{ISTD} \cdot m_S} \cdot P_{ISTD}$$

Where: n is the number of protons that give rise to the integrated signal, *Int* is the integral value of the signal used for the quantification, *MW* is the molecular weight, *m* is the weigh (mass) and *P* is the purity of the internal standard. The subscript notations are *ISTD* for the internal standard, *t* for the target analyte, and *S* for the analyzed sample.

DLS characterization of multidomain vesicles

DLS characterization on multidomain vesicles was performed after extrusion; control measurements were repeated before each experiment. ζ-potential was measured only for M1 vesicles due to the presence of the negatively charged lipid GM1 (5% mol%). All vesicle suspensions showed great colloidal stability in time.

M1		M2	M3
d_h [nm]	ζ [mV]	d_h [nm]	d_h [nm]
108.7 ± 1.4	-64 ± 3	102.8 ± 0.7	101.8 ± 0.5

Table S8. Hydrodynamic diameter (d_h) and ζ-potential (ζ) characterization of multidomain lipid vesicles with three different compositions. For DLS size results, we considered the number distributions. We calculated the uncertainty on the mean value on 12 measurements; in the case of ζ-potential, we used 9 measurements. For both hydrodynamic diameter and ζ-potential measurements, the uncertainties correspond to the 95 % confidence intervals of Student's t-distributions.

^1H NMR characterization of NP–

Control of the presence of unbound ligands. NP– (ca. 5 mg) were dispersed in MeOH-d_4 (600 µL), the sample was sonicated for 30 min and ^1H NMR spectrum was acquired. The absence of clear and sharp peaks indicates that no unbound ligands are present.

Determination of the ligand shell composition after decomposition of the gold core. NP– (ca. 5 mg) were dispersed in the etching solution (I_2 in MeOH-d_4, 0.5 mg mL^{-1}, 600 µL) and the mixture was sonicated for 30 min. A black precipitated was formed and only the clear orange solution was

transferred into 5 mm NMR tube. ^{1}H NMR spectrum was acquired (delay: 60 s, acquisition time: 4 s, number of scans: 1024). Post-acquisition processing was performed with MestReNova (Mestrelab research v. 11.0): manual phase correction, 264 k zero filling, 5rd order polynomial baseline correction, apodization LB = 0.1 Hz and manual integration. After normalization on the number of nuclei and correction due to each contribution, the integral values were used to calculate the ratio between OT and the MUS ligand, respectively. ^{1}H NMR spectrum of NP− after iodine etching is reported in Figure A17.
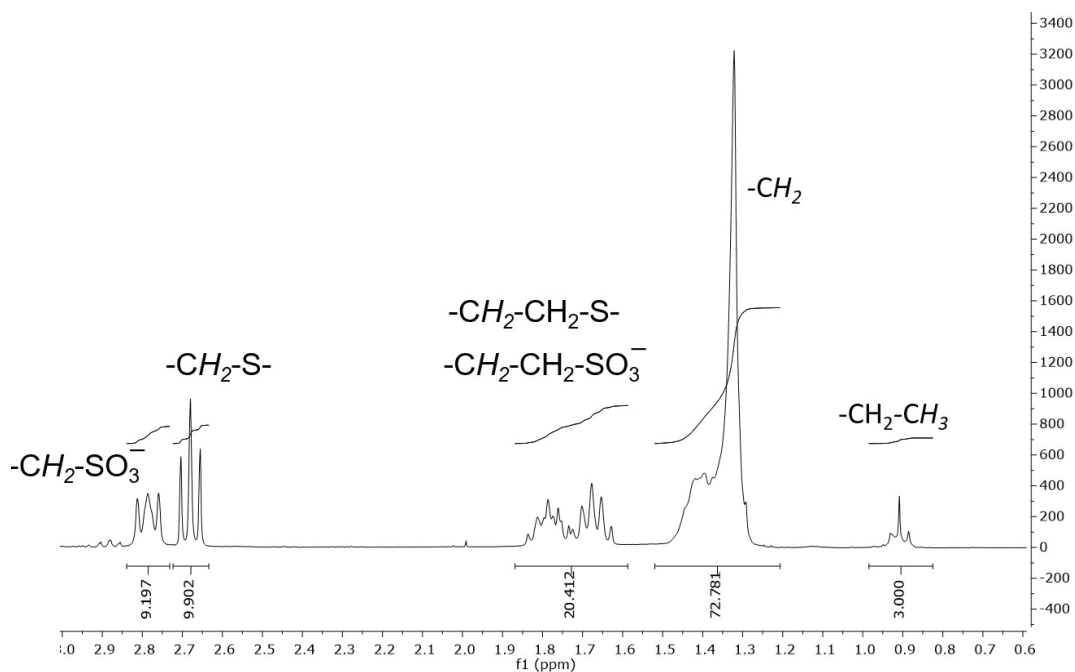
Figure S17. ^{1}H NMR characterization of NP−. Expansion of ^{1}H NMR spectrum of NP− after iodine etching in MeOH-d₄. From ^{1}H NMR analysis after decomposition, the NP− ligand shell was found to be composed of 20 % OT and 80 % MUS.

Computational results: list of unbiased molecular dynamics simulations

Start configuration	End configuration	Simulated time [μs]	#NPs	NP size [nm]
Reference M1	–	50	0	–
NP in water phase @ M1	NP fully embedded in the membrane; Lo domain dissolved	20	1	2
NP in water phase @ M1	NP adsorbed on Ld phase; Lo domain dissolved	20	1	4
NP in hydrophobic contact @M1	NP in hydrophobic contact; Lo domain dissolved	20	1	4
NP fully embedded in the Ld phase of M1	NP fully embedded in the membrane; Lo domain dissolved	20	1	4
NPs in hydrophobic contact @ M1 and far from each other	Stable dimer	10	2	4
NPs fully embedded in the M1 membrane and far from each other	Stable dimer	10	2	4
NPs fully embedded in M1 and close to each other	NPs disperse in the membrane	10	12	2
NPs fully embedded in M1 and forming a hexagonal aggregate	NPs forming the hexagonal aggregate	10	7	4
NPs fully embedded in M1, random positions	NPs forming the hexagonal aggregate	30	7	4
C_{60} fully embedded in the Ld phase of M1	NP fully embedded in the membrane; Lo domain stable	30	50	C_{60}
Reference M3	–	10	0	–
NP fully embedded in the Ld phase of M3	NP fully embedded in the membrane	20	1	4
NPs fully embedded in the Ld phase of M3	NPs fully embedded in the membrane	30	2	4

Table S9. List of unbiased simulations.

References

1   R. Bao, L. Li, F. Qiu and Y. Yang, *J. Phys. Chem. B*, 2011, **115**, 5923–5929.

2   E. Gazit, I. R. Miller, P. C. Biggin, M. S. P. Sansom and Y. Shai, *J. Mol. Biol.*, 1996, **258**, 860–870.

3   T. J. Zwang, W. R. Fletcher, T. J. Lane and M. S. Johal, *Langmuir*, 2010, **26**, 4598–4601.

4   N. Kučerka, S. Tristram-Nagle and J. F. Nagle, *J. Membr. Biol.*, 2006, **208**, 193–202.

5   L. Monticelli, *J. Chem. Theory Comput.*, 2012, **8**, 1370–1378.

6   T. A. Wassenaar, H. I. Ingólfsson, R. A. Böckmann, D. P. Tieleman and S. J. Marrink, *J. Chem. Theory Comput.*, 2015, **11**, 2144–2155.

7   Y. Ha, L. E. Katz and H. M. Liljestrand, *Environ. Sci. Technol.*, 2015, **49**, 14546–14553.

8   R. C. Van Lehn, M. Ricci, P. H. J. J. Silva, P. Andreozzi, J. Reguera, K. Voïtchovsky, F. Stellacci and A. Alexander-Katz, *Nat. Commun.*, 2014, **5**, 4482.

9   Z. P. Guven, P. H. J. Silva, Z. Luo, U. B. Cendrowska, M. Gasbarri, S. T. Jones and F. Stellacci, *J. Vis. Exp.*, 2019, e58872.

10   V. Cagno, P. Andreozzi, M. D'Alicarnasso, P. Jacob Silva, M. Mueller, M. Galloux, R. Le Goffic, S. T. Jones, M. Vallino, J. Hodek, J. Weber, S. Sen, E.-R. Janeček, A. Bekdemir, B. Sanavio, C. Martinelli, M. Donalisio, M.-A. Rameix Welti, J.-F. Eleouet, Y. Han, L. Kaiser, L. Vukovic, C. Tapparel, P. Král, S. Krol, D. Lembo and F. Stellacci, *Nat. Mater.*, 2018, **17**, 195–203.